

A parametric study of laser spot size and coverage on the laser shock peening induced residual stress in thin aluminium samples

M. Sticchi¹, P. Staron¹, Y. Sano², M. Meixner³, M. Klaus³, J. Rebelo-Kornmeier⁴, N. Huber¹, N. Kashaev¹

¹Helmholtz-Zentrum Geesthacht, Institute of Materials Research, Max-Planck-Straße 1, D-21502 Geesthacht, Germany

²Toshiba Corporation, Power and Industrial Systems Research and Development Center, 8 Shinsugita-cho, Isogo-ku, 235-8523 Yokohama, Japan

³Helmholtz-Zentrum Berlin, Department of Microstructure and Residual Stress Analysis, Hahn-Meitner-Platz 1, D-14109 Berlin, Germany

⁴Heinz Maier-Leibnitz Zentrum (MLZ), Technische Universität München, Lichtenbergstr. 1, 85748 Garching, Germany
E-mail: marianna.sticchi@gmail.com

Published in *The Journal of Engineering*; Received on 14th June 2015; Accepted on 17th June 2015

Abstract: Laser Shock Peening is a fatigue enhancement treatment using laser energy to induce compressive Residual Stresses (RS) in the outer layers of metallic components. This work describes the variations of introduced RS-field with peen size and coverage for thin metal samples treated with under-water-LSP. The specimens under investigation were of aluminium alloy AA2024-T351, AA2139-T3, AA7050-T76 and AA7075-T6, with thickness 1.9 mm. The RS were measured by using Hole Drilling with Electronic Speckle Pattern Interferometry and X-ray Diffraction. Of particular interest are the effects of the above mentioned parameters on the zero-depth value, which gives indication of the amount of RS through the thickness, and on the value of the surface compressive stresses, which indicates the magnitude of induced stresses. A 2D-axisymmetrical Finite Element model was created for a preliminary estimation of the stress field trend. From experimental results, correlated with numerical and analytical analysis, the following conclusions can be drawn: increasing the spot size the zero-depth value increases with no significant change of the maximum compressive stress; the increase of coverage leads to significant increase of the compressive stress; thin samples of Al-alloy with low Hugoniot Elastic Limit (HEL) reveal deeper compression field than alloy with higher HEL value.

1 Introduction

The use of laser-induced pressure pulses to increase the fatigue life of a metallic component by introducing compressive Residual Stresses (RS) under its surface has been developed for more than 30 years [1] and it is still under investigation since it is becoming attractive in the aerospace industry [2]. One of the keys to understand and quantify the effects of Laser Shock Peening (LSP) on fatigue life is a clear knowledge of the RS state. To predict and optimize the RS field, several experimental and analytical studies have been reported in literature, starting by the early analytical work of Ballard [3]. Braisted and Brockman [4] first introduced the finite element (FE) method to predict the RS induced by LSP using the Abaqus software in 1999. From then on, several researchers have analysed laser shock waves propagation and the resulting residual deformations and stresses [5–8]. The present work aims to build a compendium based on experimental results providing a trend of the RS introduced in thin aluminium samples via under-water LSP, for different peening parameters and aluminium alloys. The induced stress field has been measured by the use of PRISM system, which combines the Hole Drilling (HD) with Electronic Speckle Pattern Interferometer (ESPI). PRISM measures, rarely used in LSP field, have been validated by X-ray Diffraction (XRD) and correlated with numerical and analytical prediction.

2 Laser shock peening conditions

The LSP treatment was carried out at the Power and Industrial Systems Research and Development Centre of Toshiba Corporation (Japan), with an Nd:YAG pulsed laser, producing 8 ns duration pulses at wavelength of 532 nm. Using the LSP without coating configuration [9], the samples were completely under water environment while being treated with estimated plasma pressure of $P_{max} \approx 1.9$

GPa using the empirical equation $P_{max} = \sqrt{I_0 \times Z \times \frac{\alpha}{2\alpha + 3}}$

[10], where $Z = 3 \times 10^5 \text{ g/(cm}^2 \times \text{s)}$ is the shock impedance for aluminium confined in water [11] and α is a corrective factor (which corresponds to the ratio of thermal to plasma internal energy) that was estimated to be 0.2 to reproduce the experimental plasma expansion velocity [9, 12, 13].

The temporal profile of the impact pressure was determined by the Velocity Interferometer System for Any Reflector (VISAR) doppler velocimetry. The VISAR has been used for a number of decades in high-velocity impact experiments for recording the free surface velocities of a target subject to shock wave loading [14]. This technique allows to analyse shock wave propagation and deduce the plasma pressure temporal profile $P(t)$ by measuring of back free surface velocity $U_F(t)$ and using Hugoniot conservation equations $P(t) = 1/2\rho \times D \times U_F(t)$, where D is the sound velocity and ρ is the target density [15–17]. The pressure pulse calculated for a shock impact in water confinement has the shape shown in Figure 1 and has been adopted for numerical correlation. The Full Width at Half Maximum of the pressure pulse (FWHM = 12 ns), that has been used to define the duration of the numerical dynamic analysis step, is 1.5 times the laser pulse duration.

3 Residual stresses determination

3.1 Hole drilling with ESPI

The RS were measured using the PRISM system from Stresstech [18], shown in Figure 2, which combines the well-known HD technique with ESPI.

The light from a coherent laser source is split into two parts. One part illuminates the object, which is imaged by a CCD camera, the illumination beam (see Figure 2a). The second, the reference beam, passes through an optical fibre directly to the camera. The two parts of the laser beam interfere on the CCD surface to form a speckle pattern. The phase at each pixel of the camera is determined by taking images at four phase angle steps. Deformations of the

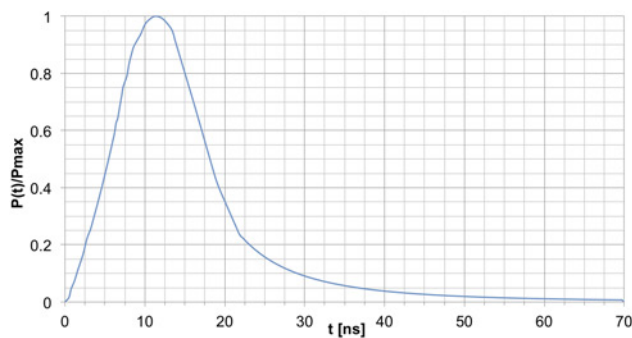


Fig. 1 Temporal profile of the impact pressure

object surface, caused by hole drilling, change the lengths of the illumination and of the object beams hence the measured phases. Subtraction of the pixel phases measured before and after drilling gives the surface displacements, from which the residual stresses can be calculated [19–21].

3.2 Validation of PRISM measurements via comparison with X-ray diffraction results

Since the combination of HD with the laser interferometer for the measures of LSP-induced RS is rare in literature [22], the measurements were validated via comparison with XRD. A comparison was done for one 2 mm thick sample of AA5083-H321 laser peened at both sides, with 40% coverage (see paragraph 4 for coverage definition) and 0.4 mm of spot diameter. The blue line in Figure 3 indicates the HD results.

The depth-resolved measurements, indicated with the black line in Figure 3, were obtained with the high-energy materials science beam-line HEMS at PETRA III using a conical slit cell [23]. The beam-line HEMS is operated by Helmholtz-Zentrum-Geesthacht (HZG) at DESY (Hamburg). A photon energy of 74.5 keV was used. The beam cross-section was $50 \times 50 \mu\text{m}$ and the depth resolution, i.e. the resolution along the beam path that was parallel to the peened surface, was 0.8 mm. The resolution perpendicular to the peened surface was thus $50 \mu\text{m}$. The sample was shifted by 2 mm parallel to the surface during exposure to improve grain statistics. The Al (311) diffraction ring was recorded on a Mar345 image plate and evaluated within 30° wide sectors using the software Fit2d [24–25]. The in-depth RS profile was measured also at the energy-

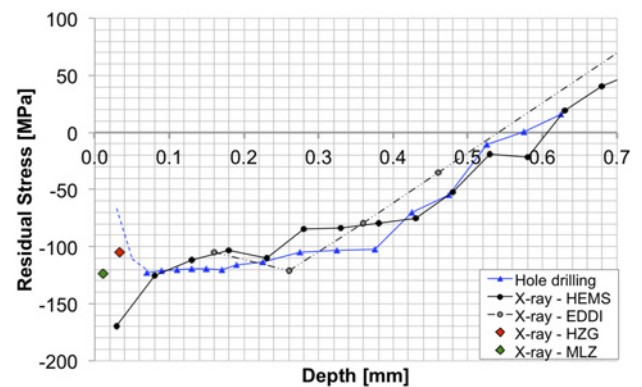


Fig. 3 Measured RS on AA5083-H321 2 mm thick sample treated with LSP at both sides

dispersive materials science beam-line EDDI, at BESSY II (Berlin), by the use of a white X-ray beam and rectangular slit cell (grey dotted line results in Figure 3). Details on the technical parameters of the beam-line are given for example in [26–28]. The measurement was performed with a gauge volume of dimensions $90 \mu\text{m} \times 940 \mu\text{m}$ and depth $150 \mu\text{m}$, at a constant 2θ angle of 11° . In order to reconstruct the profile of the RS in the thickness direction of the sample, the gauge volume was translated through the specimen along the middle scan line and at predefined sample positions. RS measurements with $\sin^2\psi$ method were performed by stepwise tilting the sample around an axis perpendicular to its length axis. The two X-ray in-depth distributions are in good agreement with the HD results except for the first point on the surface. To investigate this mismatch, surface RS measurements were carried out with a laboratory X-ray diffractometer Seifert PTS 3003 at HZG. Cu-K α radiation, a 1 mm point collimator and a linear detector were used for measuring the Al (420) reflection. The $\sin^2\psi$ method and the modulus of elasticity and Poisson's number of the bulk material were adopted for the calculation of RS. The results are shown with a red diamond in Figure 3. Further surface measurements were accomplished at the Maier-Leibnitz Zentrum of Garching by the use of a μ -X360 portable XRD residual stress analyser with $\cos\alpha$ method, with 1 mm point collimator, Cr anode, low X-ray power (30 kV, 1 mA) and full 2D sensor, giving results of illustrated by the green diamond of Figure 3 [29, 30]. To assure the reliability of the results, the sample was measured in depth at

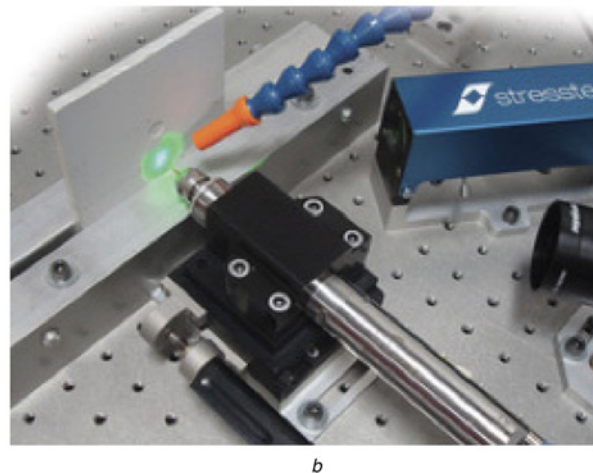
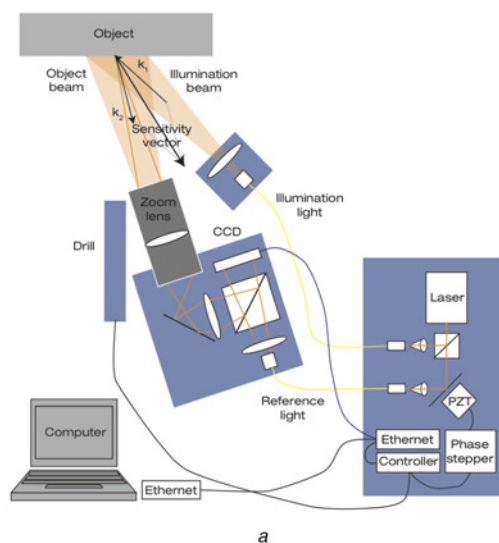


Fig. 2 Setup of the ESPI (a) and PRISM system (b) [18]

three different surface locations for each technique and the results were averaged. The X-ray in-depth RS were positioned at middle of the gauge volume and for coherence the HD results were positioned in the middle between start and end of the drilling increment.

3.2.1 Surface stress results: The surface X-ray results are plotted considering the penetration depth of the X-ray. They are in good correlation with the HD values and differ from the surface value of the in-depth synchrotron results (HEMS) of ≈ 50 MPa. Multiple laser impacts create a heterogeneous and periodic surface stress field. Since the stress value on the surface can be different from point to point, the area in which the stresses are averaged can play a significant role therefore the comparison of different surface measurements with the same techniques and, moreover, with different methods becomes very difficult.

HD with ESPI revealed some limitations near the surface. PRISM data points near the surface could tend to be closer to zero than expected. The reason could be in part addressed to the assumption of a perfectly cylindrical hole in the stress calculation [31], which is not obtained by plunge drilling using square-end end mill. In fact, an inverted cone on the bottom of the hole is created. The presence of the cone has a significant influence when the hole depth is on the order of the cone height or less, which is the case of the presented measurements. From experience with the tool, the first data point that can be considered unaffected from this and other possible source of error (e.g. surface roughness, drilling angle and zero-determination) is the point at 60 μm from the surface for a 1.2 mm end-mill diameter (cone height ≈ 30 μm). Later on, the stress at ≈ 60 μm from the surface will be indicated as “pseudo-surface” and the HD data points before 60 μm will be reported with dotted lines.

The comparison allowed to understand the capabilities of both techniques in describing the stress field due to LSP and demonstrated the reliability and reproducibility of the PRISM measures.

4 Sample features

The aluminium alloys under investigation are AA2024-T3, AA2139-T3, AA7050-T76 and AA7075-T6. The samples have

Table 1 LSP parameters of the analysed samples

Sample N°	Laser spot diameter, mm	Centres distance, mm	Coverage, %
1	0.3	0.17	40
2	0.3	0.12	60
3	0.4	0.24	40
4	0.4	0.16	60
5	0.7	0.24	60

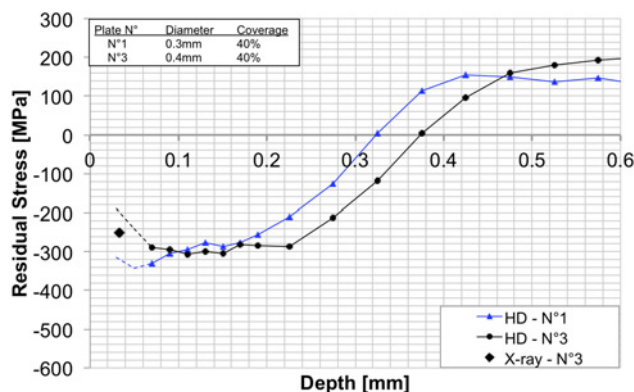


Fig. 4 HD results for 40% coverage and different spot diameters

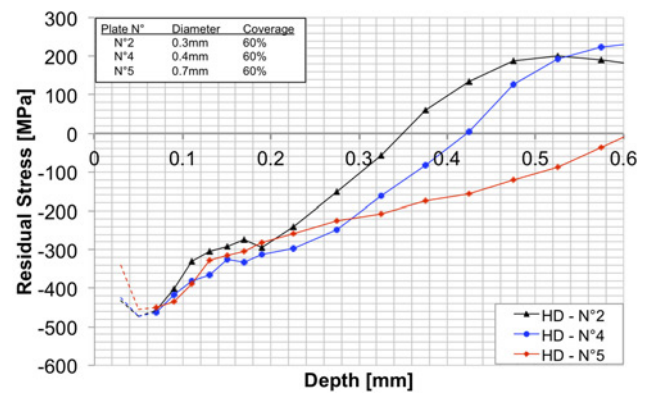


Fig. 5 HD results for 60% coverage and different spot diameters

dimensions 40 mm \times 40 mm and 1.9 mm thickness. The LSP treatment of extended areas could be achieved by the overlap of successive spots until the desired region (20 mm \times 20 mm) was completely covered. The coverage of the overlapped impacts was approximated as $\left(\frac{D-dx}{D}\right)$, where D is the impact diameter and dx is the distance between two impact centres. For each alloy 5 samples were laser-peened with different parameters, for a total number of 20 samples, summarized in Table 1.

5 Influence of spot size and coverage on residual stresses distribution

5.1 Influence of spot size

In this section we analysed the RS distribution in-depth obtained by HD measures on AA2024-T351. In Figure 4 the RS of sample N°1 and N°3, laser-peened with different spot diameters and same coverage, are compared.

It can be noted that increasing the spot size, the maximum value of the compressive stress does not change significantly. On the other hand, the zero-depth (the depth at which the compressive stress turn to tensile) increases (16%), as well as the maximum value of the tension. The surface X-ray result (performed at HZG) for sample N°3 is also reported, confirming again the good correlation with HD. The stress distributions of the two samples show a plateau of the compression at ≈ -300 MPa from the surface up to ≈ 0.18 mm for sample N°1 and up to ≈ 0.22 mm for sample N°3, suggesting that the compressive plateau becomes wider with the increase of spot size. The effect of spot size is confirmed by the comparison between samples with 60% coverage and different spot diameters, shown in Figure 5.

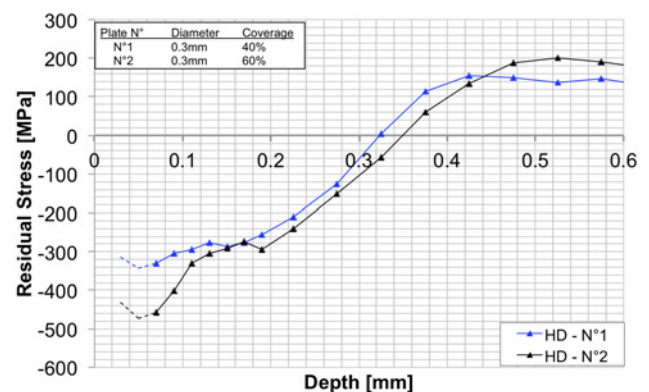


Fig. 6 HD results for 0.3 mm spot diameter and different coverage

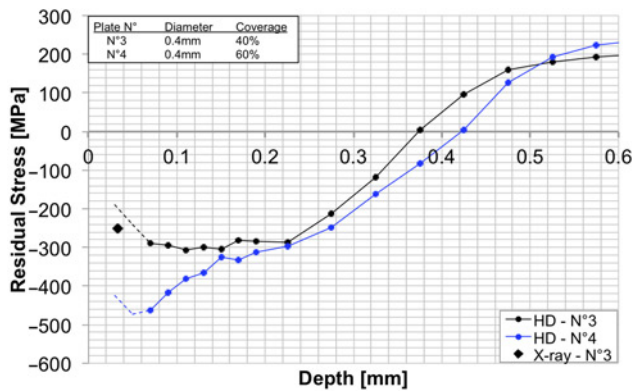


Fig. 7 HD results for 0.4 mm spot diameter and different coverage

The zero-depth value increases up to 74% from 0.3 mm to 0.7 mm spot diameter. It is possible to identify some kind of compressive plateau at ≈ -300 MPa starting from ≈ 0.1 mm under the surface. At the surface the compression is higher than the plateau value due to the effect of the higher coverage, analysed in the next section. The tension reaction of the sample N°5 was not measured due to drilling depth limitation.

5.2 Influence of coverage rate

Increasing the coverage, for the same spot diameter, Figure 6, the maximum value of compression significantly increases (38%) and as consequence also the tensile reaction increases; the zero depth also increases (8%), but much less compared to the effect of increasing spot size.

Increasing the coverage, for samples with 0.4 mm spot diameter, leads again to an increase of all the three quantities with a particular effect on the compression peak (60%), as illustrated in Figure 7.

The compression left by one impact on the near surface is added to the compression of the following impact in the overlap zone. When the coverage increases, the area of overlap is larger and then the residual compressive stresses are higher in magnitude.

5.3 Discussions

Figure 8 shows a quasi-linear variation of the zero-depth with spot size for the two different coverage. The increase of zero-depth due to less than 50% spot diameter increment (from 0.3 mm of sample N°1 to 0.4 mm of sample N°3) is higher than the increase caused by 50% coverage increment (from 40% coverage of sample N°1 to 60% of sample N°2).

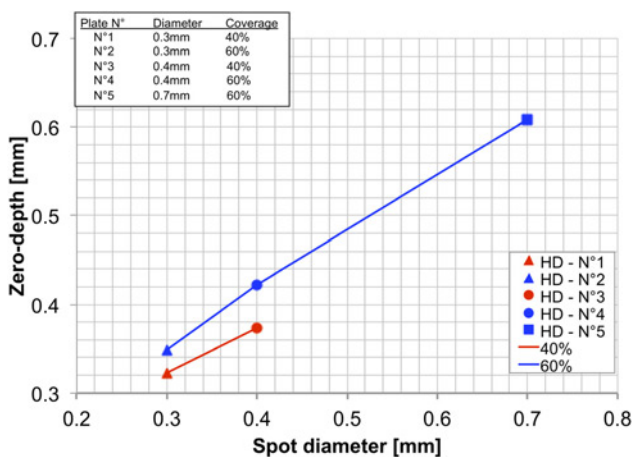


Fig. 8 Zero-depth variation with spot size and coverage

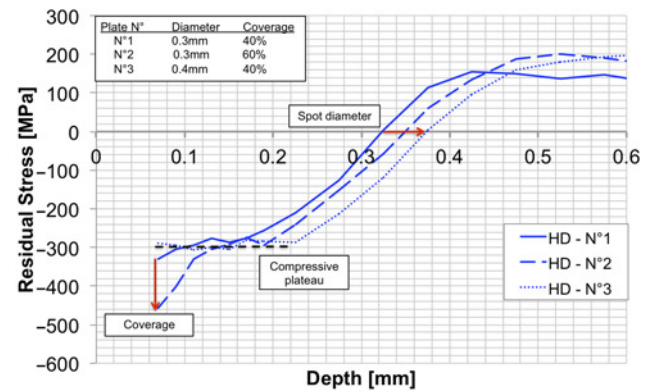


Fig. 9 RS distribution behaviour with the increase of spot diameter and coverage

The generalized RS distribution can be identified thanks to Figure 9. The increment of the spot size increases the zero-depth enlarging the compressive plateau with no significant change of the compression peak (from sample N°1 to sample N°3). On the other hand, the increment of the coverage (from sample N°1 to sample N°2), leading to a smaller increase of zero-depth, increases the compression stress near the surface. For the 40% coverage samples the stress near the surface is not significantly exceeding the compressive plateau level while for the 60% sample the RS distribution shows a peak stress near the surface. The compressive stress for 60% coverage decreases after the near surface peak reaching the compressive plateau and following afterward the 40% coverage RS in-depth profile.

6 Finite Element simulation

6.1 Finite Element model

For the purpose of correlating the experimental outcomes with fast numerical prediction, a 2D-axisymmetric FE model was developed on ABAQUSTM 6.12 Explicit software, assuming symmetric behaviour about the central axis of the model. The face opposite to the loaded surface was fixed to simulate the sample condition during the treatment. For each impact, the explicit dynamic analysis includes three steps: loading and shock propagation, relaxation and removal of constraints. 4-node axisymmetric solid elements, having elastic-plastic behaviour, were used to mesh the area under the impact, while for the surrounding zone 4-node axisymmetric infinite elements, with elastic behaviour, were adopted providing “quiet” boundaries to the finite area. The infinite elements are located at the side of the finite region, orthogonal to the main direction of the wave propagation [32]. The finite element region used for a single impact is chosen three times larger than the laser spot to fully include the RS zone [33, 34]. A schematic of the model is shown in Figure 10.

Since in dynamic analyses results are sensitive to the mesh configuration a convergence analysis was carried out for different meshes, described in Table 1, in order to select the correct element size for the finite region. The mesh density is defined as a ratio of element length (L_e) to radius of impact zone (r_p) [35]. A moderate mesh refinement was selected providing accurate results and computational efficiency.

During the simulation with a fine mesh, the current temperature at the loaded surface can exceed the melting temperature. This gave unrealistic results because in that case the material behaves as fluid [36]. The reason is, that the fast energy input leads to an adiabatic heating of the material. Increasing the mesh refinement, the high temperature gradients are then resolved by the numerical simulation, delivering such high temperatures. In reality, the melting temperature is never exceeded since the loaded surface is cooled

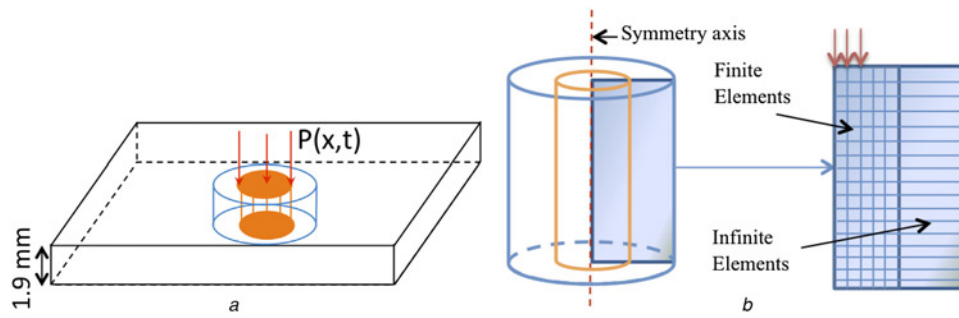


Fig. 10 (a) Idealisation of the single laser impact; (b) detailed view of finite and infinite regions

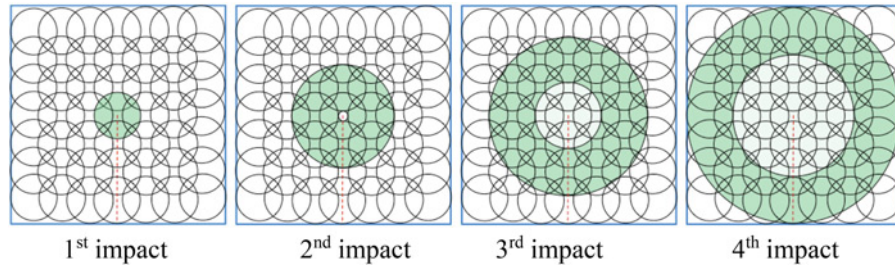


Fig. 11 Multiple impacts simulated as rings around the centre of the model

by water. Since the temperature dependence and the water-cooling are neglected in the presented simulation, the melting temperature has been set high to avoid such effects.

The explicit FE method is conditionally stable [37, 38]. To ensure the stability of the analysis, the integration time has been set one order of magnitude smaller than the critical value (being approximately equal to the time for an elastic wave to cross the smallest element). The duration of the loading step was set three orders of magnitude longer than the FWHM of the pressure pulse to allow the plastic deformation to occur in the material [35, 39]. The relaxation step and the step in which constraints are removed were set twice the loading step.

6.2 Material behaviour

The Johnson-Cook plasticity model is one of the most frequently used models for impact studies [33, 40, 41] and has been adopted

for the present simulation. The model describes the flow stress as a product of three terms: a strain hardening, a strain-rate dependent and a temperature term:

$$\sigma = [A + B\epsilon^n] \left[1 + C \ln \left(\frac{\dot{\epsilon}}{\dot{\epsilon}_0} \right) \right] \left[1 - \left(\frac{T - T_0}{T_{melt} - T_0} \right) \right]$$

The expression in the first set of brackets gives the stress as a function of strain for $\frac{\dot{\epsilon}}{\dot{\epsilon}_0} = 1.0$ and $\frac{T - T_0}{T_{melt} - T_0} = 0$. The expression in the second and third sets represents the effects of strain rate and temperature. T_0 , T and T_{melt} are respectively the room temperature, current temperature and melting temperature. The value of the strain rate sensitivity parameter (C) was taken as average of the values found in literature for aluminium alloys ($C=0.01$). ϵ and $\dot{\epsilon}$ denote respectively the true plastic strain and the true plastic strain rate. The true plastic strain rate $\dot{\epsilon}_0$ is the rate used to determine A , B and n via the quasi-static tensile tests. Logically $\dot{\epsilon}_0$ must be consistent with the choice of the yield and hardening parameters [42].

For each material about 6 specimens were tested by quasi-static tensile tests (3 in transverse and 3 in longitudinal direction) with good reproducibility of the results. The values of the static yield stress (A) and of the elastic modulus (E) were determined from

Table 2 Configurations for mesh sensitivity

Element length, L_p , mm	Mesh density, L_e/r_p %
0.02	10 (coarse)
0.01	5 (moderate)
0.005	2.5 (fine)

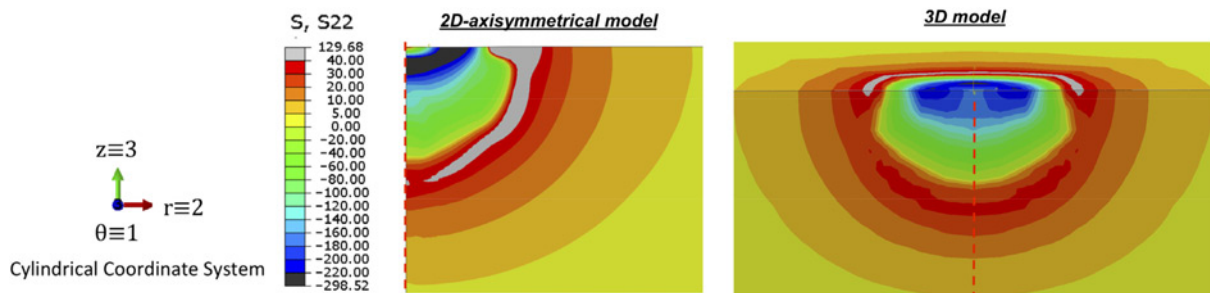


Fig. 12 RS induced by a single impact simulated by 2D-axisymmetrical and 3D model

Table 3 Mechanical properties of AA2024-T351, AA2139-T3, AA7050-T76 and AA7075-T6.

Aluminium alloy (AA)	Density, ρ [g/cm ³]	Elastic modulus, E [MPa]	Poisson's ratio, ν	Static yield stress, A [MPa]	Strain hardening exponent, n	Strength Coefficient, B [MPa]	True strain rate, $\dot{\epsilon}_0$ [s ⁻¹]
2024-T351	2.78	74326	0.33	350	0.73	972	0.000199
2139-T3	2.80	72130	0.33	363	0.83	846	0.000098
7050-T76	2.83	69347	0.33	532	0.67	497	0.000303
7075-T6	2.81	73934	0.33	529	0.59	519	0.000285

the resulting true σ - ϵ curves together with the strain hardening exponent (n) and the strength coefficient (B). In fact, in the strain hardening region (from $R_{p0.2}$ to the onset of necking) the true σ - ϵ curve can be approximated by the equation $\sigma = B\epsilon^n$, which in logarithmic form, $\log\sigma = \log B + n\log\epsilon$, is a straight line where n is the slope and $\log B$ is the y-intercept. The mechanical properties of the studied aluminium alloys are illustrated in Table 2. The densities were taken from [43, 44].

6.3 Simulation of a single and multiple laser impacts

A pressure load was used to simulate the plasma pressure resulting from the laser pulse impact. In order to evaluate the pressure spatial distribution, the numerical deformations were compared with experimental surface deformations from literature [45, 46]. A spatial profile with a Gaussian equation to the power of 6 avoids displacement discontinuity at the border of the loaded surface area without modifying the RS field with respect to uniform spatial distribution.

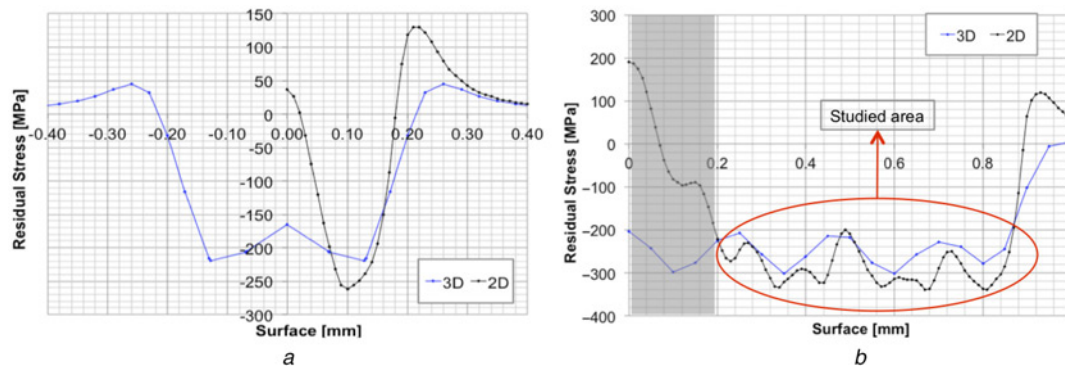
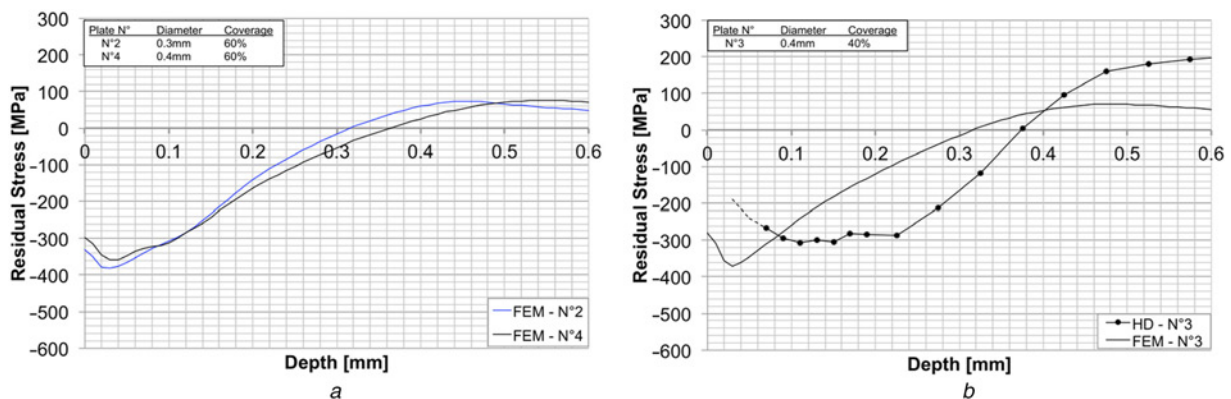
In the analysis of multiple impacts, for simplification related to the adoption of the 2D-axisymmetrical model, the impacts following the first central one are simulated as rings around the centre as

schematically shown in Figure 10 for a sequence resulting in 40% coverage.

To confirm the validity of the model, a 3D FE model was developed and compared. The 3D model is composed by 8-node solid elements and was meshed with the smallest element being 0.05 mm long in an area close to the impact. Multiple impacts are applied as single circular impacts one next to the other. The stresses induced under the surface by a single laser impact for both models are illustrated in Figure 12. The resulting stress distributions are discussed in the next section.

6.4 Numerical prediction of residual stresses

Both models present a reduced stress level at the surface in the centre of a single circular impact, as shown in Figure 12 and in Figure 13 (a); this can be understood from the interaction and reflection of release waves [47]. In fact, when the laser beam impacts the surface, the sudden rise of plasma pressure creates a plane longitudinal wave at the surface, which propagates into material. At the border of the impact, two types of release waves are created: a longitudinal and a transverse wave, occurring at the side of the impact. The interaction of the transverse release wave with the surface

**Fig. 13** Surface RS induced by single (a) and multiple impacts (b), simulated with 2D-axisymmetrical and 3D model**Fig. 14** Influence of spot size on numerical RS distributions (a); comparison between experimental and numerical results (b)

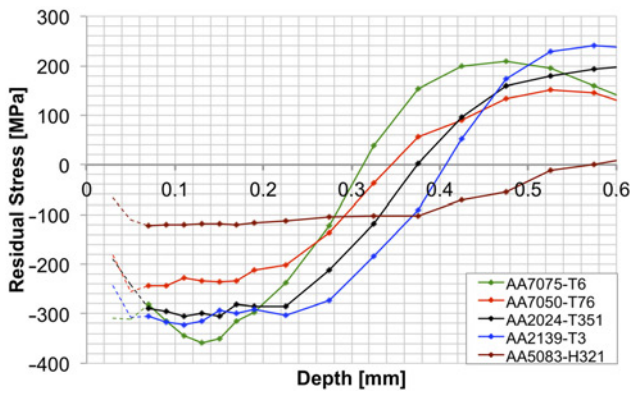


Fig. 15 HD experimental RS distribution for different materials

creates a Rayleigh wave. As the Rayleigh wave approaches the centre of the impact, it induces a V-shaped plastic deformation of the surface near the centre of the impact zone. After the passage of the Rayleigh wave, the bulk of the substrate tends to react against the deformation created in the surface layer, flattening the V shape [48]. As consequence of the material reaction, the stress drops at the centre of the impact.

The 2D model is more sensitive to this effect, which is likely due to the finer mesh. In fact, previous FE investigation revealed that for an explicit dynamic analysis the stress drop at the impact centre is more evident when a finer mesh is used. It has been observed that the V-shaped plastic deformation is larger and deeper when a larger spot is used.

This observation suggests that deeper compressive RS (i.e. higher value of the zero-depth) are achievable with a larger spot size.

Comparing the results of the two models, there is a good match of the RS distribution in-depth and at the surface except in the centre of the entire peened area, not considered in the analysis (grey zone in Figure 13b). The prediction at the centre of the peened area in the axisymmetric model can be unrealistic due to the repeated waves focusing phenomenon that affects the centre of the specimen model for every ring that is added. Considering the similar RS prediction, the 2D model is convenient in terms of computational costs (the 3D analysis is ≈ 30 times longer than the 2D for multiple impacts simulating 40% coverage).

The numerical simulation predicts the effects of spot size and coverage found experimentally. Figure 14a, for example, shows the increase of zero-depth with the spot size and the small variation of the compression peak. Each in-depth curve has been averaged from two surface locations, at the impact centre and at the overlap.

Comparing the experimental with the simulation results in Figure 14b, it can be seen that the residual stress profile from the simulation is shifted to lower depth by about 100 μm with a consequent underestimation of the zero-depth and of the tension reaction.

7 Zero-depth and pseudo surface stress for different materials

The HD measured in-depth RS distribution of all the studied aluminium alloys are represented in Figure 15 for samples N°3 (0.4 mm spot diameter and 40% coverage). The AA5083-H321 results, previously shown in paragraph 3.2, have been added to Figure 15 for comparison.

In order to catch information about the variation of the zero-depth and the surface stress for same LSP parameters and different materials, a summary of the available numerical and experimental zero-depth values vs the Hugoniot Elastic Limit (HEL) of the different materials, for the samples N°3, is illustrated in Figure 16. The red triangles and the blue circles indicate respectively the HD and the

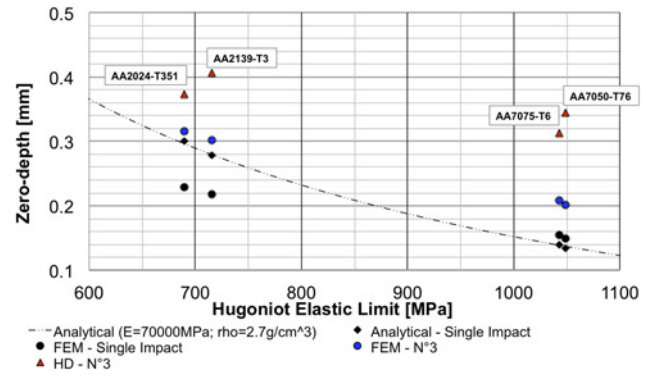


Fig. 16 Numerical, analytical and experimental values of zero-depth vs HEL

FE results. The numerical results for one peen and the analytical results from the well-known Ballard model [3, 48, 50] are also illustrated with black points. Even though the numerical prediction underestimate the experimental values, it is possible to identify the same trend: LSP treatment of a material with low HEL, and therefore low yield strength, can produce higher values of the zero-depth than a material with higher HEL for the same peening conditions. The ratio between experimental and numerical results is in average ≈ 1.4 and with respect to one peen the ratio is ≈ 2 . By multiplying the zero-depth obtained from the simulation for one impact by this ratio, a first estimation of the zero-depth achievable with coverage of 40% rate can be obtained.

Figure 17 is a compendium of the available numerical and experimental surface stress values vs the HEL. As already seen, the FE model (blue circles) well predicts the pseudo-surface stress measured by HD (red triangles).

The analytical trend of the surface stress, for one impact, has been obtained by modifying in the Ballard formulation [3] the hypotheses of $L_p \ll r_0$ into $L_p \sim r_0$ (studied case). The resulting equation is

$$\sigma_{surf} = \frac{3}{2} \left(\frac{\mu \varepsilon_{pl}}{1 - \nu} \right) \left[1 - \frac{3(1 + \nu)}{2\pi} \frac{L_p}{r_0 \sqrt{2}} \right]$$

where, μ and ν are respectively a Lamé constant and the Poisson ration, ε_{pl} is the plastic deformation, r_0 is the impact radius and L_p is the plastic affected depth (here assumed to be comparable to the zero-depth). The analytical σ_{surf} linearly depends on ε_{pl} that has a maximum (plastic saturation value) when the applied peak pressure is twice the HEL. For the AA2024-T351 and AA2139-T3 alloys the plastic saturation value has been reached. This

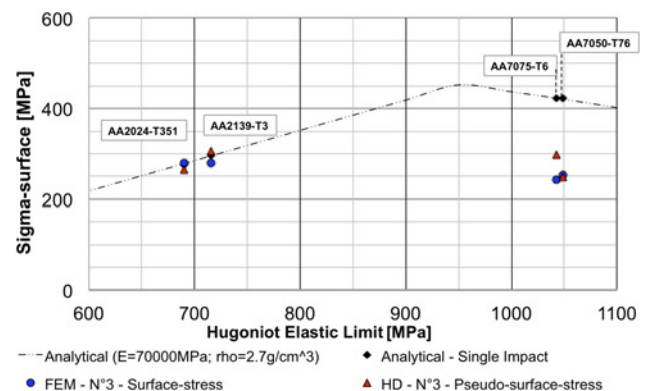


Fig. 17 Numerical, analytical and experimental values of surface stress vs HEL

explains the slope change of the analytical curve in Figure 17 at $HEL = P_{\max}/2 = 950 \text{ MPa}$.

8 Conclusions

Laser shock peened specimens of 1.9 mm thickness, produced from aluminium alloys AA2024-T351, AA2139-T3, AA7050-T76 and AA7075-T6 have been analysed with more than 30 HD measurements. The ESPI was used in combination with HD to measure the RS. The results were validated with XRD experiments and correlated with numerical and analytical predictions. The information derived from the great amount of results has been discussed and the main outcomes can be summarised as follows:

- The values of zero-depth, which gives an indication of the amount of residual compression through the thickness, increases significantly when a large spot size is used, without significant change of maximum compression stress.
- In order to increase the maximum value of compression, which gives an indication of the magnitude of RS after peening, the most efficient solution is to increase the coverage.
- By peening an alloy with low HEL (therefore low yield strength) it is possible to obtain deeper compression field, increasing the value of the surface stress by optimising the applied pressure.
- For a first estimation of the achievable results, a fast and simple 2D-axisymmetrical model can be used. The results of one single impact can be scaled with a factor that has been derived from the comparison with experimental results for various aluminium alloys to predict the effect of coverage.

9 Acknowledgment

The first author acknowledges Dr R. Ecourt from the Department of Physics and Mechanics of Materials of the Institute PPRIME of Poitiers, for VISAR experiments, and Dr T. Rickert from the American Stress Technologies society for the valuable discussion on PRISM system.

10 References

- [1] Hackel L.A., Chen H.L.: LS&T Annual Report 2001, UCRL-ID-134972-01, Springfield, VA 22161, USA
- [2] Sticchi M., Schnubel D., Kashaev N., Huber N.: 'Review of residual stress modification techniques for extending the fatigue life of metallic aircraft components', *Appl Mech Review*, 2015, **67**, pp. 010801–1–9, doi:10.1115/1.4028160
- [3] Ballard P.: 'Contraintes résiduelles induites par impact rapide. Application au choc laser'. PhD Thesis, Ecole Polytechnique, 1991
- [4] Braisted W., Brockman R.: 'Finite element simulation of laser shock peening', *International J Fatigue*, 1999, **21**, pp. 719–724
- [5] Zhang W., Yao Y.L., Noyan I.C.: 'Microscale laser shock peening of thin films, Part I: experiment, modeling and simulation', *J Manuf Sci Eng*, 2004, **126**, pp. 10–17, doi:10.1115/1.1645878.
- [6] Ocana J.L., Molpeceres C., Porro J.A., Gomez G., Morales M.: 'Experimental assessment of the influence of irradiation parameters on surface deformation and residual stresses in laser shock processed metallic alloys', *Appl Surf Sci*, 2004, **238**, pp. 501–505
- [7] Hu Y.X., Yao Z.Q.: 'FEM simulation of residual stresses induced by laser shock with overlapping laser spots', *Acta Metall. Sin*, 2008, **21**, (2), pp. 125–132
- [8] Peyre P., Chaieb I., Braham C.: 'FEM calculation of residual stresses induced by laser shock peening in stainless steels', *Modelling Simul. Mater. Sci. Eng.*, 2007, **15**, pp. 205–221, doi:10.1088/0965-0393/15/3/002
- [9] Sano Y., Akita K., Masaki K., Ochi Y., Altenberger I., Scholtes B.: 'Laser peening without coating as a surface enhancement technology', *JLMN*, 2006, **1**, (3), pp. 161–166
- [10] Fabbro R., Fournier J., Ballard P., Devaux D., Virmont J.: 'Physical study of laser-produced plasma in confined geometry', *J. Appl. Phys.*, 1990, **68**, pp. 775–784, doi:10.1063/1.346783

- [11] Lee K., Lim C.H., Kwon S.O.: 'Propagation of laser-generated shock wave in a metal confined in water', *J. of the Korean Physical Society*, 2006, **49**, (1), pp. 387–392
- [12] Sano Y., Mukai N., Yoda M., Ogawa K., Suezono N.: 'Underwater laser shock processing to introduce residual compressive stress on metals', *Material Science Research International*, 2001, Special Technical Publication, **2**, pp. 453–458
- [13] Devaux D., Fabbro R., Tollier L., Bartnicki E.: 'Generation of shock waves by laser-induced plasma in confined geometry', *J Appl. Phys.*, 1993, **74**, pp. 2268–2273, doi:10.1063/1.354710
- [14] Barker L.M.: 'VISAR vs PDV', *Valyn International*, <http://www.valynvisar.com/>, accessed April 2015
- [15] Berthe L., Fabbro R., Peyre P., Tollier L., Bartnicki E.: 'Shock waves from a water-confined laser-generated plasma', *J Appl. Phys.*, 1997, **82**, (6), pp. 2826–2832, doi: 10.1063/1.366113
- [16] Romain J.P., Darquey P.: 'Shock waves and acceleration of thin foils by laser pulses in confined plasma interaction', *J. Phys. Appl. Phys.*, 1990, **68**, pp. 1926–1928, doi:10.1063/1.346587
- [17] Peyre P., Berthe L., Fabbro R., Sollier A.: 'Experimental determination by PVDF and EMV techniques of shock amplitudes induced by 0.6–3 ns laser pulses in a confined regime with water', *J. Phys. Appl. Phys.*, 2000, **33**, pp. 498–503
- [18] <http://www.stresstechgroup.com/>, accessed April 2015
- [19] Nelson D.V.: 'Residual stress determination by hole drilling combined with optical methods', *Experimental Mechanics*, 2010, **50**, pp. 145–158, doi:10.1007/s11340-009-9329-3
- [20] Jacquot P.: 'Speckle interferometry: a review of the principal methods in use for experimental mechanics applications', *The Author J. compilation*, 2008, Strain 44, pp. 57–69
- [21] Schajer G.S.: 'Advances in hole-drilling residual stress measurements', Proceedings of the XIth International Congress and Exposition, Orlando, Florida, June 2008
- [22] Coratella S., Sticchi M., Toparli M.B., Fitzpatrick M.E., Kashaev N.: 'Application of the eigenstrain approach to predict the residual stress distribution in laser shock peened AA7050-T7451 samples', *Surface and Coatings Technology*, 2015, **273**, pp. 39–49, doi:10.1016/j.surfcoat.2015.03.026
- [23] Staron P., Fisher T., Keckes J., Schratter S., Hatzenbichler T., Schell N., Mueller M., Schreyer A.: 'Depth-resolved residual stress analysis with high-energy synchrotron X-rays using a conical slit cell', *Mater. Sci. Forum*, 2014, **768–769**, pp. 72–75
- [24] Hammersley A.P.: 'FIT2D: An Introduction and Overview', ESRF Internal Report, 1997, ESRF97HA02 T
- [25] Hammersley A.P., Svensson S.O., Hanfland M., Fitch A.N., Häusermann D.: 'Two-dimensional detector software: from real detector to idealised image or two-theta scan', *High Pressure Research*, 1996, **14**, pp. 235–248
- [26] Genzel C., Denks I.A., Gibmeier J., Klaus M., Wagener G.: 'The materials science synchrotron beamline EDDI for energy-dispersive diffraction analysis', *Nucl. Instrum. Methods in Phys. Research A*, 2007, **578**, pp. 23–33
- [27] Meixner M., Klaus M., Genzel C.: 'Sin²ψ-based residual stress gradient analysis by energy-dispersive synchrotron diffraction constrained by small gauge volumes. I. Theoretical concept', *J. Appl. Cryst.*, 2013, **46**, pp. 610–618
- [28] Meixner M., Klaus M., Genzel C.: 'Sin²ψ-based residual stress gradient analysis by energy-dispersive synchrotron diffraction constrained by small gauge volumes. II. Experimental implementation', *J. Appl. Cryst.*, 2013, **46**, pp. 619–627
- [29] <http://www.pulstec.net/>, accesses June 2015
- [30] Miyazaki T., Sasaki T.: 'X-ray stress measurement with two-dimensional detector based on Fourier analysis', *Int. J. Mater. Res.*, 2014, **105**, (9), pp. 922–927
- [31] Schajer G.S., Prime M.B.: 'Use of inverse solution for residual stress measurement', *Journal of Engineering Materials and Technology*, 2006, **128**, (3), pp. 375–382
- [32] Tae Keun Oh: 'Defect characterization in concrete elements using vibration analysis and imaging', PhD Thesis, University of Illinois Urbana-Champaign, 2012
- [33] Amarchinta H.K., Grandhi R.V., Langer K., Stargel D.S.: 'Material model validation for laser shock peening process simulation', *Modelling Simul. Mater. Sci. Eng.*, 2009, **17**, doi:10.1088/0965-0393/17/1/015010
- [34] Braisted W., Brockman R.: 'Finite element simulation of laser shock peening', *International Journal of Fatigue*, 1999, **21**, pp. 719–724
- [35] Ding K., Ye L.: 'Laser shock peening: performance and process simulation', Woodhead Publishing Limited, 2006
- [36] ABAQUS Analysis User's manual, 1998

- [37] Wriggers P.: 'Nonlinear finite element methods', Springer editor, 2008
- [38] Zienkiewicz O.C., Taylor R.L.: 'The Finite Element Method', Fifth Edition, Butterworth-Heinemann editors, 2000
- [39] Berthe L., Fabbro R., Peyre P., Bartnicki E.: 'Wavelength dependent of laser shock-wave generation in the water-confinement regime', *Int. J. Appl. Phys.*, 1999, **85**, pp. 7552–7555, doi:10.1063/1.370553
- [40] Zerilli F.J., Armstrong R.W.: 'Dislocation-mechanics-based constitutive relations for material dynamics calculations', *J. Appl. Phys.*, 1987, **61**, pp. 1816–1825, doi:10.1063/1.338024
- [41] Johnson G.R., Cook W.H.: 'A constitutive model and data for metal subjected to large strains, high strain rates and high temperatures'. Proc. Seventh Int. Symp. on Ballistics, The Hague, Netherlands, 1983, pp 541–547
- [42] Schwer L.: 'Optional strain-rate forms for the Johnson Cook constitutive model and the role of the parameter epsilon_0¹'. Proc. Sixth German LS-DYNA Users' Forum, Frankenthal, Germany, 2007, (E-I)1–14
- [43] <http://asm.matweb.com/>, accessed April 2015
- [44] <http://www.matweb.com/>, accessed June 2015
- [45] Song H.B., Peyre P., Ji V., Jiang C.H.: 'Near surface stress gradients analysis by gixrd on laser shocked 6056 aluminium alloy samples', *International Centre for Diffraction Data*, 2009, pp. 485–492
- [46] Hfaiedh N., Peyre P., Popa I., Vignal V., Seiler W., Ji V.: 'Experimental and numerical analysis of the distribution of residual stresses induced by laser shock peening in a 2050-T8 aluminium alloy', *Material Science Forum*, 2011, **681**, pp. 296–302
- [47] Forget P., Strudel J.L., Jeandin M., Lu J., Castex L.: 'Laser shock surface treatment of Ni-based superalloys', *Mater Manufact Processes*, 1990, **5**, (4), pp. 501–528, doi:10.1080/10426919008953275
- [48] Dubrujeaud B., Fontes A., Forget P., Papaphilippou C., Sainte-Catherine C., Vardavoulas M., Jeadin M.: 'Surface modification using high power laser: influence of surface characteristics on properties of laser processed materials', *Surf Eng*, 1997, **13**, (6), pp. 461–470
- [49] Ballard P., Fournier J., Fabbro R., Frelat J.: 'Residual stresses induced by laser-shocks', *J Phys IV*, 1991, **1**, (C3), pp. 487–494
- [50] Peyre P., Fabbro R., Merrien P., Lieurade H.P.: *Mater Sci Eng A*, 1996, **210**, (1–2), pp. 102–113